Digital Object Identifier (DOI): 10.1109/TIA.2016.2633539

IEEE Transactions on Industry Applications

Quad-Active-Bridge DC–DC Converter as Cross-Link for Medium-Voltage Modular Inverters

Levy Ferreira Costa
Giampaolo Buticchi
Marco Liserre

Suggested Citation

L. F. Costa, G. Buticchi and M. Liserre, "Quad-Active-Bridge DC–DC Converter as Cross-Link for Medium-Voltage Modular Inverters," in IEEE Transactions on Industry Applications, vol. 53, no. 2, pp. 1243-1253, March-April 2017.

Quad-Active-Bridge DC-DC Converter as Cross-Link for Medium Voltage Modular Inverters

Levy Costa, *Student Member, IEEE,* Giampaolo Buticchi, *Member, IEEE,* and Marco Liserre, *Fellow, IEEE*

***Abstract*—One of the main challenges of the solid-state transformer (SST) lies in the implementation of the dc-dc stage. In this paper, a Quadruple-Active-Bridge (QAB) dc-dc converter is investigated to be used as basic module of a modular three-stage SST. Besides the feature of high power density and soft-switching operation (also found in others converters), the QAB converter provides a solution with reduced number of high frequency transformers, since more bridges are connected to the same multi-winding transformer. To ensure soft-switching for the entire operation range of the QAB converter, the triangular current mode modulation strategy, previously adopted for the dual-active-bridge converter, is extended to the QAB converter. The theoretical analysis is developed considering balanced (equal power processed by the MV cells) and unbalanced (unequal power processed by the MV cells) conditions. In order to validate the theoretical analysis developed in the paper, a 2 kW prototype was built and experimented.**

***Index Terms*—Dc-dc converter, multiwinding transformer, solid-state transformer, triangular current modulation.**

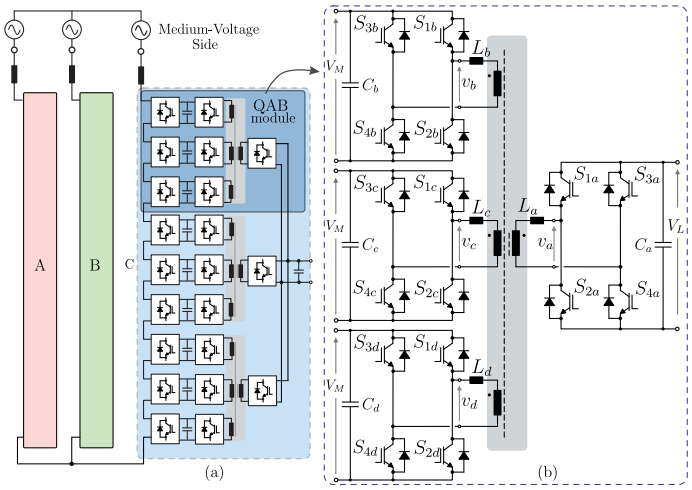

Fig. 1. (a) Modular SST architecture using the QAB converter as a basic module of the dc-dc stage and (b) QAB topology.

I. Introduction

In recent years, several smart grid technologies have received attention, as a possible solution to manage in an efficient way the growth in load and the high penetration of distributed generation. One of these technologies is the Solid-State Transformer [1]–[8]. This power electronics based system uses a high frequency (HF) transformer, reducing volume and space, and it can also provide ancillary services to the grid, such as: reactive power injection on the MV side, dual micro-grid operation [7], load identification and control [9], storage integration, management of hybrid grids (dc and ac) and power quality improvement.

The three-stage SST, chosen for the availability of the dc-connection and for the superior grid service respect to two or single-stage architectures [7], is composed of a Medium-Voltage (MV) ac-dc stage, a HF isolated dc-dc stage and a Low-Voltage (LV) dc-ac stage. The main challenge of this architecture is the dc-dc conversion stage, since it has strict requirements: high rated power, high current capability in LV side, high voltage capability in HV side, high frequency isolation and high efficiency. To meet all requirements, two solutions have been widely investigated: the first one is to use a converter with high voltage rating devices [10]–[12], while the second one is based on the modular concept, in which several modules are used to share the total voltage and power among them [2], [13]–[15]. Although the modular solution presents a high number of components, it has several advantages, such as: low dv/dt (low EMI emission and isolator stress), possibility to use standard low voltage rating devices and also modularity, which allows to implement redundant strategy to increase the fault tolerance and reliability.

Several converters have been investigated to be used as module of the main core of the SST, but the Dual-Active-Bridge (DAB) and the Series-Resonant converter (SRC) have received more attention, due to their advantages of soft-switching, high efficiency and high power density [13]–[19].

The Multiple Active Bridge (MAB) is an alternative solution to the DAB or SRC. This kind of converter was firstly introduced in [20] and it was applied in [21] to connect renewable energy sources and storage systems.

The use of MAB to realize the dc-dc stage (Fig. 1) of the SST leads to a reduced number of transformers and modules, when compared to the design based on DAB, while still preserving the same advantages. Moreover, the QAB has the possibility to exchange power among the modules of the MV inverter directly through the HF transformer, because of the cross connection configuration of this converter. Therefore, the QAB converter can be defined as a "cross-link" for the modules of MV modular inverter. The possible power paths among the cells of the QAB converter are depicted in Fig. 2, where the feature of power exchange among the MV cells is highlighted.

This paper will investigate the operation of the QAB using the triangular current modulation (TCM) scheme in the SST system, in which the impact on the converter power and control stages is evaluated for balanced and unbalanced conditions. In section II, the operation principle of the converter using the TCM is described in detail and all equations are derived. The

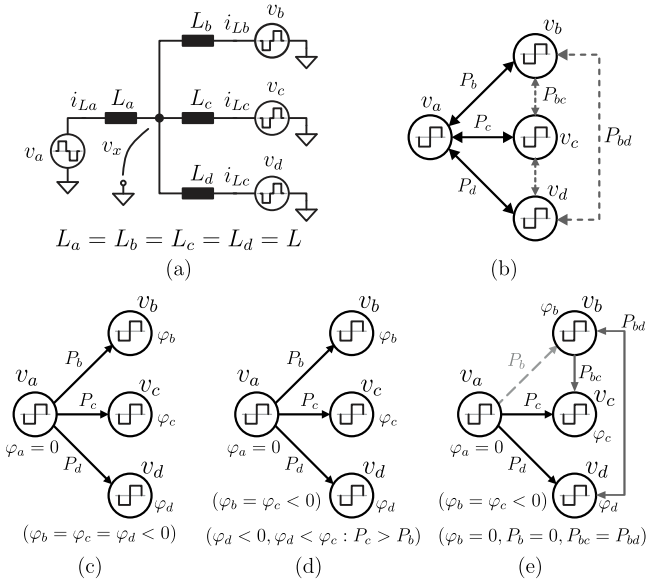

Fig. 2. Equivalent circuit of the QAB converter (a) and possible power transfer paths among the actives bridges: (b) all possible power paths. (c) Usual balanced condition case, where the LV cell a delivers equal power to the three MV cells (b, c and d), (source: cell a, load: cell b, c and d). (d) Usual unbalanced condition case, where the LV cell a delivers different powers to the MV cells (b, c and d), and in this example the cell d receives more power than the cells b and c; (source: cell a, load: cell b, c and d). (e) Unusual case, where the MV cell b operates as a source, giving energy to cells (b and c), (source: cell a and b, load: cell c and d). In the last case, $P_1 = 0$.

semiconductors and transformer current stresses are evaluated in section III. The control scheme and the strategy to manage the unbalanced condition are discussed in section IV. In section V, the design procedure and simulation results of the QAB are presented, while experimental results are discussed in section VI.

II. Operation Principle

The QAB is composed by four active bridges and for the analysis, each of them is denoted by a, b, c and d. The elements of the bridges have subindex $i = \{a, b, c, d\}$ to indicate the bridge the element belongs to, as depicted in Fig. 1 (b). In SST application, the bridge a is connected to the LV side, while the bridges b, c and d are connected to the MV side. All bridges can exchange power among them and the possible power paths are depicted in Fig. 2 (b), where each bridge is symbolized by the voltage source v_i.

To analyze the converter, an equivalent circuit based on the Y-model and depicted in Fig. 2 (a) is used, in which the bridges are replaced by rectangular voltage sources (v_a, v_b, v_c and v_d). The voltage on the central point v_x and the current slope of each inductor are given by (1) and (2), respectively.

$$v_x = \frac{v_a + v_b + v_c + v_d}{4} \tag{1}$$

$$\frac{di_{Li}}{dt} = \frac{(v_i - v_x)}{L} \tag{2}$$

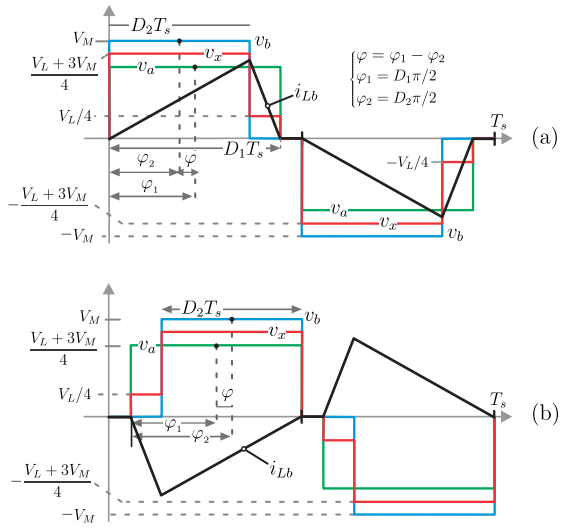

Fig. 3. Main waveforms of the QAB converter: (a) positive power flow (from MV to LV side), (b) negative power flow (from LV to MV side).

A. Triangular Current Modulation Strategy

Originally, the classical phase-shift modulation strategy has been applied to most multiple active bridge solutions present in literature [20], [21]. In this scheme, rectangular voltages v_a, v_b, v_c and v_d with phase shift φ_a, φ_b, φ_c and φ_d, respectively, and constant switching frequency f_s are applied to the transformer. The power is controlled by the phase difference among the bridges. As a disadvantage of this strategy, high level of reactive power circulates in the high frequency transformer when the phase-shift operation angle is high. Besides that, the soft-switching range of the PSM is limited.

The TCM, introduced in [22], presents an attractive solution to modulate the QAB converter. Differently from the PSM strategy, the TCM uses the duty-cycle to control the power transferred among the bridges. Using the TCM, the switches of the MV cells can operate with ZCS and the circulating reactive power on the converter can be reduced. This strategy has been intensively investigated for the DAB converter [23], [24] and in this paper, it is extended to the QAB converter.

Firstly, it is considered that the QAB converter operates in balanced condition, i.e. $P_b = P_c = P_d$ and the LV bridge duty-cycle is given by D_1, while the duty-cycles of the MV cells b, c and d are given by D_2, D_3 and D_4, respectively. As the balanced condition is assumed, then $D_2 = D_3 = D_4$.

The basic principle of the TCM is to impose a triangular current on the inductors, as shown in Fig. 3. To achieve that, the voltages v_a and v_b should have the waveforms depicted in Fig. 3 (a) and consequently the voltage v_x is

$$v_x = \begin{cases} \dfrac{nV_L + 3V_M}{4}, & 0 < t < d_2T_s \\ \dfrac{nV_L}{4}, & d_2T_s < t < d_1T_s \\ 0, & d_1T_s < t < T_s/2 \end{cases} . \tag{3}$$

As can seen in Fig. 3 (a), the current in the inductor starts from zero and reaches its maximum value Δi_{Lb} during the

period of time between $0 < t < D_2T_s$, where T_s is the switching period. The current variation during this period, denoted as $\Delta i_{Lb_{(0<t<D_2Ts)}}$, can be calculated by using (2), where v_x is given by (3), resulting in (4). As the currents start from zero, the switches S_2 and S_3 of the LV side and also the switches S_5 and S_6 of the MV side turn-on at zero current switching (ZCS).

$$\Delta i_{Lb_{(0<t<D_2Ts)}} = \frac{D_2\left(V_M - nV_L\right)}{4Lf} \tag{4}$$

Likewise, during the period $D_2T_s < t < T_s/2$, the currents decrease from Δi_{Lb} until reaches zero again. For this period, the current variation denoted as $\Delta i_{Lb_{(D2Ts<t<Ts/2)}}$ can also be calculated by (2), resulting in (5). In the moment $t = D_2T_s$, the current is zero and the switch S_1 turns-off at ZCS. It is important to note that the period in zero state should be long enough to deplete all charge accumulated in the IGBT during the conduction state. Thus, this commutation can be critical for rated load operation, where the stored charge is high and the zero time period is small [23]. To achieve ZCS operation regardless the load and input or output voltages levels, the condition $\Delta i_{Lb_{(0<t<D2Ts)}} = \Delta i_{Lb_{(D2Ts<t<Ts/2)}}$ must be satisfied. As a results, the relation between the duty-cycle D_1 and D_2 is found and presented in (6).

$$\Delta i_{Lb_{(D_2Ts<t<Ts/2)}} = \frac{nV_L\left(D_1 - D_2\right)}{4Lf_s} \tag{5}$$

$$D_2 = \frac{V_L \cdot n}{V_M} D_1 \tag{6}$$

B. Power Transfer

The transferred power can be calculated at the dc side of the bridges by: $P_{i(avg)} = I_i V_i$. The average current in the cell b (I_b) is calculated in (7). Thus, the powers processed by the cell b (MV cell) and a (LV cell) are shown in (8).

$$I_b = \frac{2}{T_s}\int_0^{D_2T_s} i_b\left(d\right)dt \;=\; \frac{{D_2}^2\left(V_M - nV_L\right)}{4Lf_s} \tag{7}$$

$$P_b = \frac{{D_1}^2(V_Ln)^2\left(V_M - V_Ln\right)}{4Lf_sV_M}$$

$$P_a = \frac{3{D_1}^2(V_Ln)^2\left(V_M - V_Ln\right)}{4Lf_sV_M} \tag{8}$$

As can be observed in (8), the duty-cycle of the cell a, D_1 is used to control the power transferred, while the duty-cycle of the MV cells ($D_{2,3,4}$) are used to ensure the ZCS operation.

C. Influence of the Transformer Parasitic Elements

The previous analysis was performed considering the ideal transformer case, where all the leakage inductances are assumed to be equal ($L_a = L_b = L_c = L_d$), in order to simplify the analysis and derive all the equations in a didactic approach. However, in practical application, deviation in the stray inductance of the transformer is expected, mainly because of the manufacturing process. The real model of the transformer is depicted in Fig. 4 (a), where the leakage inductance, coil resistance and parasitic capacitance among the windings are observed. Therefore, the analysis of the QAB considering a different leakage inductance for each transformer winding is performed.

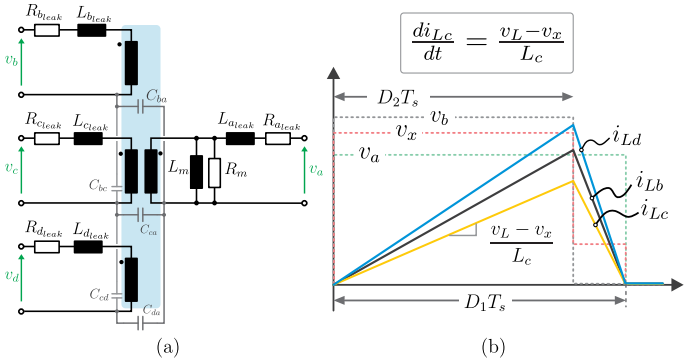

Fig. 4. Model of the HF transformer, considering its non-ideal elements.

Initially, it is analyzed the effect of different winding leakage inductance on the ZCS operation of the QAB converter. It is assumed that the winding connected to the bridge b has the expected leakage inductance ($L = L_b$), while the inductances of the bridge c and is 10% higher than expected and the indutance of the bridge d is 8% lower than the expected value. Therefore: $L = L_b = 1.1 \cdot L_c = 0.92 \cdot L_d$ and the expected current waveforms are presented in Fig. 4 (b).

Analyzing the current on the bridge c (i_{Lc}) and using the equation (2), the current variation during the first and second periods are given by (9) and (10), respectively.

$$\Delta i_{Lc_{(0<t<D_2Ts)}} = \frac{D_2\left(V_M - nV_L\right)}{4f_s(1.1L)} = \frac{\Delta i_{Lb_{(0<t<D_2Ts)}}}{1.1} \tag{9}$$

$$\Delta i_{Lc_{(D_2Ts<t<Ts/2)}} = \frac{nV_L\left(D_1 - D_2\right)}{4f_s(1.1L)} = \frac{\Delta i_{Lb_{(D_2Ts<t<Ts/2)}}}{1.1} \tag{10}$$

Since it is assumed that the equation (6) is satisfied, the equation (11) is found and, therefore, the condition to achieve ZCS operation is still valid. It means that a difference on transformer stray inductance has no effect on the ZCS operation of the converter.

$$\Delta i_{Lc_{(0<t<D_2Ts)}} = \Delta i_{Lc_{(D_2Ts<t<Ts/2)}} \tag{11}$$

On the other hand, a deviation on the transformer leakage inductances will have some impact on the amount of transferred power to the ports. As can be observed in Fig. 4 (b), the area below the current changes according to the inductance and consequently the transferred power also changes. Analyzing the circuit shown in Fig. 2 (a), the voltage v_x is described by

$$\frac{{v_a}' - v_x}{{L_a}'} + \frac{v_b - v_x}{L_b} + \frac{v_c - v_x}{L_c} + \frac{v_d - v_x}{L_d} = 0 \tag{12}$$

Taking into account the waveforms of the voltages v_a and v_b, solving (12) and using the same analysis approach described for the ideal case (the intermediates steps are omitted), the variation of the current i_c can be calculated by (13), while the power transferred to the port c is computed (14).

$$\Delta i_{Lc} = \frac{L_bL_d\left(nV_L\right)\left(D_1 - D_2\right)}{f_s\left[{L_a}'L_b\left(L_c + L_d\right) + \left({L_a}' + L_b\right)L_cL_d\right]} \tag{13}$$

$$P_c = \frac{D_1^2 L_b L_d (nV_L)^2 (V_M - nV_L)}{V_M f_s \left[L_a{}' L_b (L_c + L_d) + (L_a{}' + L_b) L_c L_d\right]}. \quad (14)$$

Finally, equation (14) shows the complete power transfer equation of the QAB converter using TCM, considering different inductances. Considering 10% of deviation on the inductance L_c ($L = L_b = 1.1 \cdot L_c = L_d$) and replacing these values in (14), it is found (15). From this equation, it is observed that 10% of deviation in one stray inductance affects only 2.5% of the transferred power.

$$P_c = 1.025 \cdot \frac{D_1^2 (nV_L)^2 (V_M - nV_L)}{4 L f_s} = 1.025 \cdot P_b \quad (15)$$

Since the effect of inductance deviation is small, the ideal analysis can also be used in many cases.

III. Semiconductors and Transformer Efforts

In order to evaluate the performance in term of efficiency of the QAB converter using the TCM scheme, the current effort on the semiconductors and transformer are calculated. The current waveforms on the transformer primary side and on the semiconductors of the LV bridge and MV bridge are depicted in Fig. 5 (a). As can be noticed in this figure, the LV side switches commutate at ZCS during the turn-on and turn-off. For the switches of the MV cell, the i_{S2b} has ZCS during the turn-on and turn-off, while the switch i_{S1b} has ZCS only during the turn-on.

Based on the curves presented in Fig. 5 (a), the rms currents on the primary and secondary side of the transformer in function of the duty-cycle D_1 are calculated by (16) and (17), respectively.

$$i_{Lb,rms} = \frac{nV_L (V_M - nV_L)}{12 L f_s V_M} \sqrt{6 {D_1}^3} \quad (16)$$

$$i_{La,rms} = \frac{n^2 V_L (V_M - nV_L)}{4 L f_s V_M} \sqrt{6 {D_1}^3} \quad (17)$$

The rms and average currents through the semiconductors of the LV bridge are given by (18) and (19), respectively.

$$i_{S_1 a,rms} = \frac{n^2 V_L (V_M - nV_L)}{4 L f_s V_M} \sqrt{3 {D_1}^3} \quad (18)$$

$$i_{S_1 a,agv} = \frac{3 {D_1}^2 \left(n^2 V_L\right) (V_M - nV_L)}{8 L f_s V_M} \quad (19)$$

Similarly, the rms and average currents through the switch S_{1b} of the MV cells are given by (20) and (21), respectively, while the effort the switch S_{2b} are given by (22) and (23).

$$i_{S_{1b},rms} = \frac{nV_L (V_M - nV_L)}{12 L f_s V_M} \sqrt{\frac{3 {D_1}^2 n V_L}{V_H}} \quad (20)$$

$$i_{S_{1b},agv} = \frac{{D_1}^2 (nV_L)^2 (V_M - nV_L)}{8 L f_s {V_M}^2} \quad (21)$$

$$i_{S_{2b},rms} = \frac{nV_L (V_M - nV_L)}{12 L f_s V_M} \sqrt{3 {D_1}^3} \quad (22)$$

$$i_{S_{2b},agv} = \frac{{D_1}^2 (nV_L) (V_M - nV_L)}{8 L f_s V_M} \quad (23)$$

Fig. 5 (b) shows the graphic of the current effort through the semiconductor and transformer in function of the output power of the QAB converter. The graphics were obtained using the previous equations and the follow parameters: $V_L = 700V$, $V_M = 1130V$, $f_s = 20kHz$, $D_{1_{max}} = 0.48$, $L = 12.5uH$ and $n = 1.3$. The calculation of the parameters is explained in detail in Section V (A. Design Procedure).

IV. Control System

A. Unbalanced Condition

For unbalanced condition ($P_b \neq P_c \neq P_d$), the duty-cycles of the MV bridges are not equal anymore. The duty-cycle of each MV cell will depend on the processed power. For this

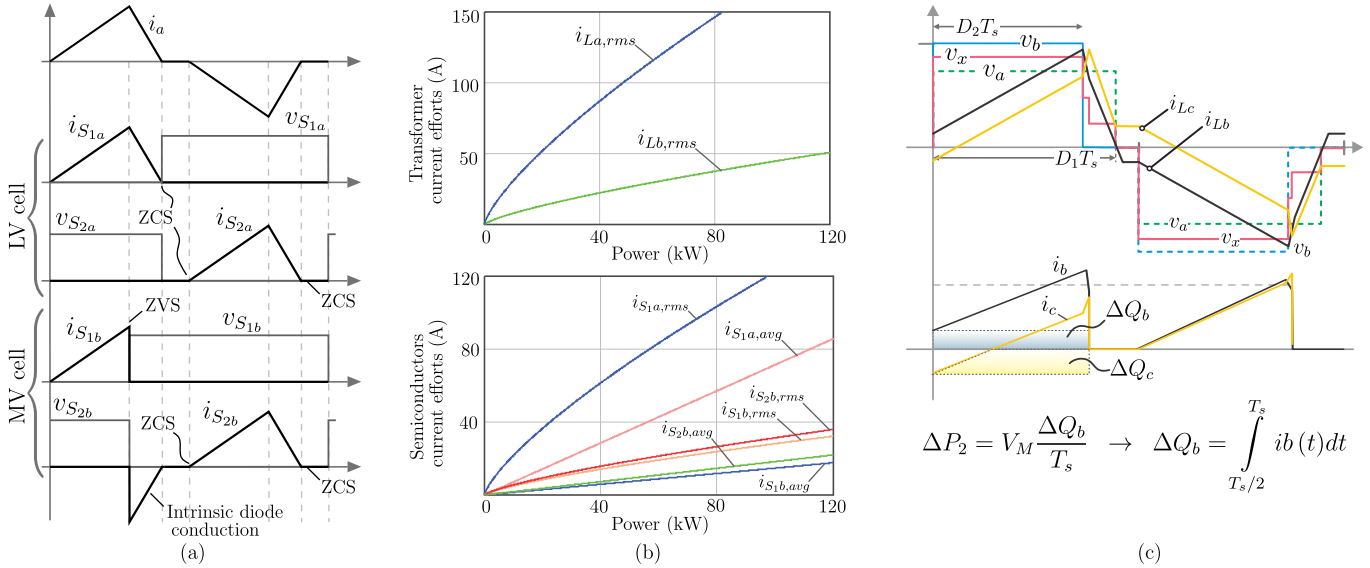

Fig. 5. (a) Current waveform on the semiconductors and transformer of the QAB converter, (b) current stresses (rms and average) on the semiconductor and transformer in function of the total transferred power and (c) main waveforms of the converter for unbalanced condition, considering positive power flow.

analysis, it is considered that only the power of the cell b is different, i.e. $P_b \neq P_c = P_d$. Considering this condition, the voltages v_a, v_b and v_x, as well as the current i_{Lb} and i_{Lc} are depicted in Fig. 5 (c). As can be observed in this figure, the voltage v_x has one more level, caused by the duty-cycle difference given by $\Delta D_2 = D_3 - D_2$. This additional level makes the current i_b decrease and the current i_c increase. Afterwards, both currents decrease with the same slope, but they reach different values, since they started from different points. As a conclusion, the variable ΔD has direct impact on the dc value of the currents, and consequently the additional power delivered by the MV cell. For that reason, this new variable can be used to control the power exchange among the MV cells, as described in [25].

The dc side current waveforms of the cells b and c are also depicted Fig. 5 (c). As it can be seen, the output current of the ports is affected by the unbalanced condition only during half switching period. Besides that, the additional amount of charge delivered or removed from each port is highlighted in the figure.

$$P_b = \frac{P_a}{3} + \Delta P_b \tag{24}$$

To calculate the imbalance effect on the power processed of the MV cells, it is assumed that the power of the cell b is composed of the total balanced power (given by $P_a/3$) and an additional power portion ΔP_b, as presented in (24). Thus for balanced condition $\Delta P_b = 0$. The additional power ΔP_b is calculated using the additional charge (ΔQ_b and ΔQ_c) as shown in Fig. 5. Therefore, it is found the equation of ΔP_b in function of ΔD_2, as presented in (25). The same procedure can be applied to the power transferred by the cell c and the results is given by (26). As can be observed in (25) and (26), the equations of the additional power are in function of ΔD_2. This variable can be used to control the additional power transferred to the MV bridges.

$$\Delta P_b = \frac{3{V_M}^2 \Delta D_2 \left(D_2 - \Delta D_2\right)}{2Lf_s} \tag{25}$$

$$\Delta P_c = \frac{3{V_M}^2 \Delta D_2 \left(\Delta D_2 - D_2\right)}{4Lf_s} \tag{26}$$

Fig. 6 shows the current effort on the semiconductors of the cells b and c, when the QAB converter operates with TCM and an unbalanced condition of 15% (i.e. one MV cell processing 15% more power then the others) and 30%, in order to point out the imbalance on the semiconductors effort.

B. Control Structure

To control the converter two control loops are used: output voltage control (LVDC link control) and power balance control. The control scheme used in this converter has the same concept of the structure described in detail in [26], but it was adapted for the TCM. Fig. 7 shows the block diagram of the employed control structure and it is briefly described here.

The LVDC link loop is used to control the output voltage and is responsible for the total amount of power transferred

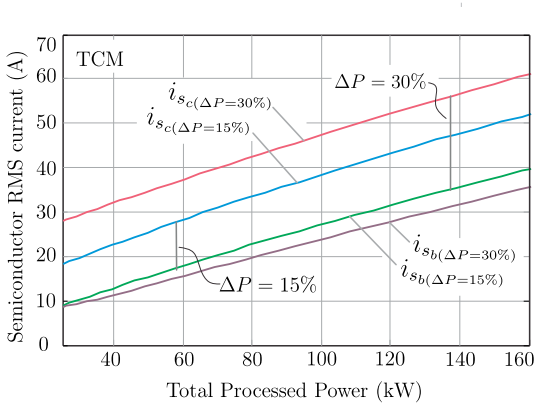

Fig. 6. Semiconductors effort of the QAB converter for unbalanced condition of 15% and 30%.

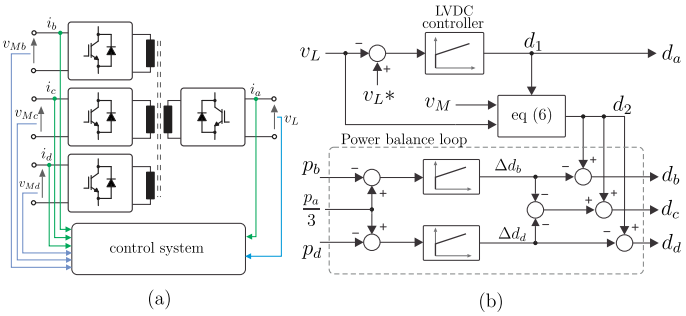

Fig. 7. Control structure: (a) measured parameters of the QAB converter and (b) simplified block diagram of the control scheme.

from the MV side to the LV side, by using the variable d_1, as described in Section III.

To ensure the same amount of power processed by the MV bridges, a power balance loop is used. The duty-cycle of the MV bridges are calculated using (6) to achieve the ZCS condition. Besides that, the variable ΔD is used to balance the power. Therefore, the duty-cycle of each bridge is composed by two variables: d_2, responsible to ensure ZCS condition, and Δd_k (where $k = b, c, d$), responsible to balance the power. The correlation between the variable Δd_k and the amount of additional transferred power to each MV bridge is presented in (25) and (26).

V. Design Procedure and Simulation Results

To validate the theoretical analysis described in this paper, a design procedure is presented in order to show how to size the main components of the converter and a simulation using the obtained parameters from the design is running in order to evaluate numerically the performance of the converter.

TABLE I
Specification of the Smart Transformer

Parameters	Value
Output nominal power	$S_{SST} = 1$ MVA
MV grid (input voltage)	$V_{MVac} = 10$ kV
LV grid (output voltage)	$V_{LVac} = 400$ V
MV dc link	$V_{MVDC} = 10.2$ kV
LV dc link	$V_{LVDC} = 700$ V

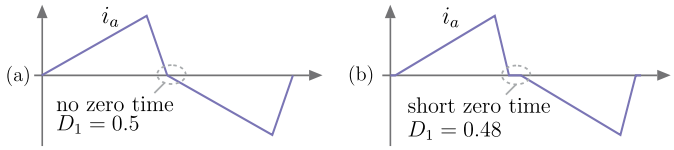

Fig. 8. Inductor current: (a) when $D_1 = 0.5$ and there is no zero time of the current, (b) when $D_1 = 0.48$ and there is a short zero time of the current.

A. Design Procedure

The design procedure is performed considering the full-scale smart transformer, whose specifications are shown in Table I and whose architecture is illustrated in Fig. 1.

In the proposed SST architecture, three QAB are used per phase, resulting in a total of nine modules. This number was chosen to have a good trade-off between number of components and effort, as demonstrated in [27]. Although this amount of modules might seem unrealistic from the practical viewpoint, there are already some industry products based also on nine modules per phase, as can be observed in [14]. In addition, the research and development of industries is also going in the direction to use more modules with reduced voltage devices, as can be observed [28], where solutions based on 1.7kV IGBT with more modules are being investigated to replace 6.5kV IGBT-based solutions.

As can be observed, the system is composed by three dc-dc converter per phase, resulting in a total of nine converters for the three-phase system ($n_{QAB} = 9$). Therefore, taking into account the grid specification shown in I and the number of converters, the specifications of a individual QAB converter are: $P_{QAB} = P_{SST}/n_{QAB} = 1MW/9 = 111.1kW$, $V_L = V_{LVDC} = 700V$; $V_M = V_{MVDC}/n_{QAB} = 10.3kV/9 = 1130V$.

The selected switching frequency is $f_s = 20$ kHz. The nominal duty-cycle D_1 can be arbitrarily chosen and the maximum value that it can assume is $D_1 = 0.5$. On one hand, if $D_1 = 0.5$ is chosen as nominal duty-cycle, it leads to reduced efforts on the semiconductors and transformer, since a large amount of power can be transferred with lower peak current on the inductors. On the other hand, the inductor current will not have a zero time, as illustrated in Fig. 8 (a), and then the ZCS can be compromised, as described in [25] and [23]. Therefore, a nominal duty-cycle of $D_1 = 0.48$ is chosen, in order to let a small zero time (see Fig. 8 (b)) to ensure the ZCS operation.

The selected transformer turns ratio is $n = 1.3$. Thus, taking into account all the defined parameters and using equation (8), the required inductances can be calculated, as presented in (27).

$$L = \frac{3D_1^2(nV_L)^2(V_M - nV_L)}{4f_sP_a}$$

$$L = \frac{3(0.48 \cdot 1.3 \cdot 700)^2(1130 - 1.3 \cdot 700)}{4 \cdot (20 \cdot 10^3) \cdot (111 \cdot 10^3)} = 12.5\mu H \tag{27}$$

The MV side inductors are $L_b = L_c = L_d = L = 12.5\mu H$, while for the LV side inductor, the turns ratio must be take into account $L_a = L/n^2 = 12.5\mu H/(1.3)^2 = 7.4\mu H$. To ensure ZCS operation, the equation (6) must be satisfied and, therefore the duty-cycle of the MV bridges D_2 is obtained, as shown in (28).

$$D_2 = D_1\frac{nV_L}{V_M} = 0.48\frac{1.3 \cdot 700}{1130} = 0.386 \tag{28}$$

The rms current on the LV side and MV side on the transformer are obtained by replacing the calculated parameters in the equations (16) and (17), respectively, as can be observed in (29).

$$i_{Lb,rms} = \frac{1.3 \cdot 700\,(1130 - 1.3 \cdot 700)}{12 \cdot (12.5\mu) \cdot (20 \cdot 10^3) \cdot 1130}\sqrt{6 \cdot 0.48^3}$$

$$i_{Lb,rms} = 47.97A$$

$$i_{La,rms} = \frac{(1.3)^2 \cdot 700\,(1130 - 1.3 \cdot 700)}{12 \cdot (12.5\mu) \cdot (20 \cdot 10^3) \cdot 1130}\sqrt{6 \cdot 0.48^3} \tag{29}$$

$$i_{La,rms} = 187.06A$$

Likewise, the current effort on the semiconductors are calculated using equations and the previous calculated parameters. The individual calculation is not presented because of space limitation and the results are summarized in the Table II.

TABLE II
COMPARISON ON THE TRANSFORMER AND SEMICONDUCTORS STRESSES DETERMINED ANALYTICALLY AND BY NUMERICAL SIMULATIONS

Parameters	Calculated (A)	Simulated (A)	Deviation (%)
$i_{La,rms}$	187.06	187.6	0.289
$i_{Lb,rms}$	47.97	48.1	0.271
$i_{S1a,rms}$	132.273	132.657	0.29
$i_{S1a,avg}$	79.286	79.595	0.387
$i_{S1b,rms}$	30.44	30.5	0.197
$i_{S1b,avg}$	16.37	16.4	0.183
$i_{S2b,rms}$	33.9	33.98	0.236
$i_{S2b,avg}$	20.33	20.41	0.394

B. Simulation Results

To verify the converter's performance and the validity of the theoretical analysis developed in this paper, the converter was simulated using the MATLAB/Simulink and the PLECS toolbox, considering the parameters presented in Table I. The results consists in steady-state operation in balanced and unbalanced condition, with the aim to verify the basic operation and the soft-switching feature of the converter described in section II. Besides that, sensitivity to parameters variation, in this case transformer leakage inductance, is also evaluated, in order to attest the analysis presented in section II *C - Influence of the Transformer Parasitic Elements*. Finally, dynamic operation is also evaluated for balanced and unbalanced power condition and all the results are summarized in Fig. 9 and 10.

1) Steady-state: Simulation results for the QAB dc-dc converter operating in balanced steady-state condition with rated power (i.e. 111.1 kW) are presented in 9 (a) to (c). The aim of these results is to demonstrate the basic operation of the

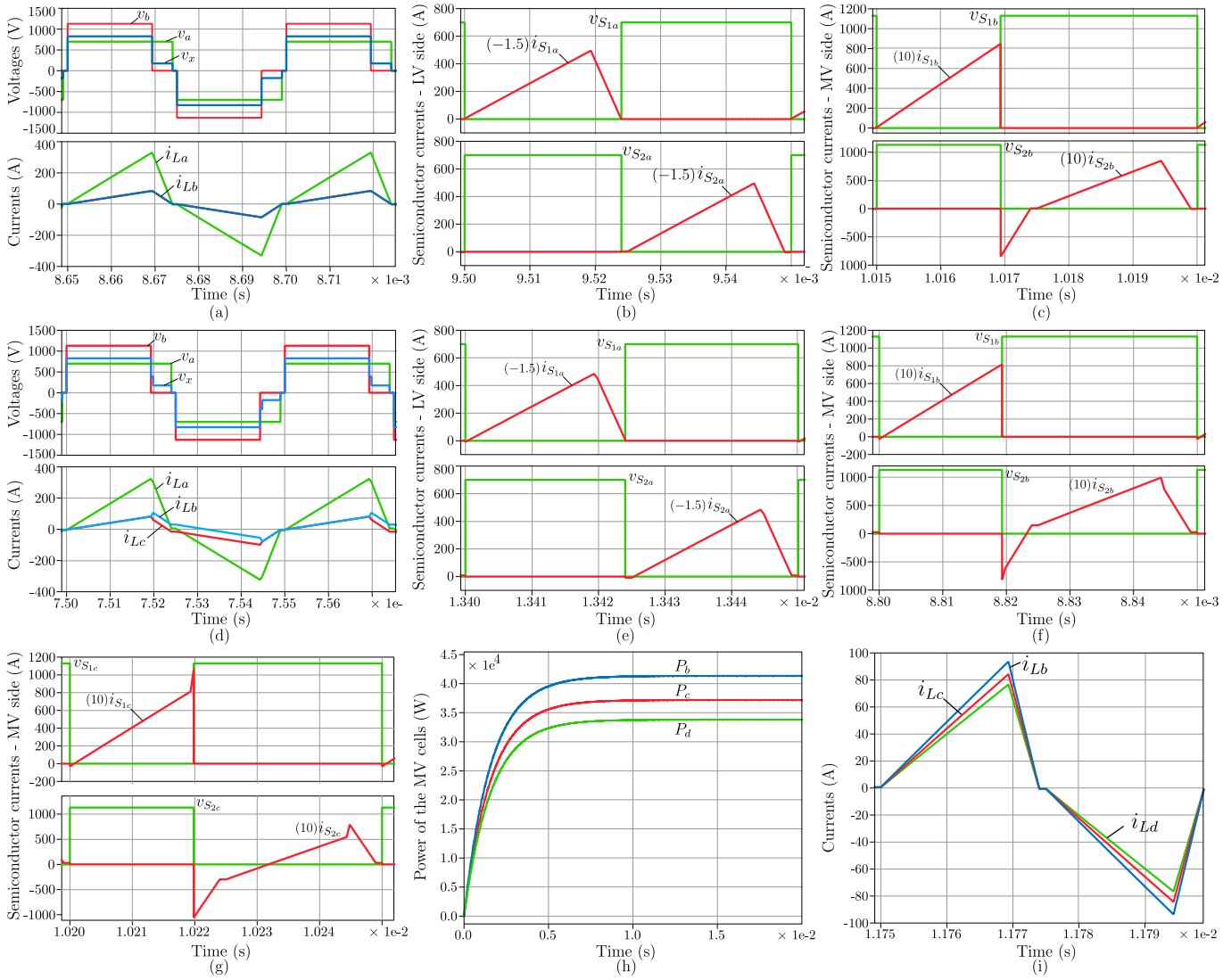

Fig. 9. Simulation results for steady-state operation: (a) main waveforms for balanced condition (v_a, v_b, v_x, i_{La} and i_{Lb}), (b) voltage and current on the semiconductors of the LV side and (c) MV side for balanced condition. (d) Main waveforms for unbalanced condition ($P_c = P_d = 42kW$ and $P_b = 24kW$), (e) voltage and current on the semiconductors of the bridge a (LV side), (f) bridge b and (g) bridge c for unbalanced condition. (h) Effect on output power of MV bridges and (i) inductors currents on the MV side for a deviation on the leakage inductance.

converter using the proposed TCM analyzed in section II. In Fig. 9 (a), the voltages v_a, v_b and v_x and the currents i_{La} and i_{Lb} are shown in agreement with the theoretical waveforms illustrated in Fig. 3 (a). As can be observed in this result, the duty-cycle of the bridge a (LV side) is $D_1 = 0.48$, while the MV bridges has the same duty-cycle of $D_2 = 0.386$. The current and voltage waveforms on the semiconductors of the LV side (bridge a) and MV side (bridge b) are depicted in Fig. 3 (b) and (c), respectively, where soft-switching operation is clearly observed. To verify the validity of all derived equations, the transformer and semiconductors stresses obtained with simulation are compared to the calculated values, as shown in Table II. This comparison shows a very good accuracy of the analytical equations, proving their validity.

2) Unbalanced load condition: Likewise, Fig. 9 (d) to (e) shows the same main waveforms for unbalanced load condition. These results were obtained for the converter operating with bridges c and d processing $42kW$, while bridge b operates with power level of $24kW$ In Fig. 9 (d), the imbalance can be clearly observed on the waveform of the voltage v_x, in which more levels are present, and also on the waveforms of the currents i_{Lb} and i_{Lc}. The additional level on the voltage v_x has a duration determined by $\Delta D = D_2 - D_3$ and, due to this level, the current i_{Lb} increases instead to decrease, while the current i_{Lc} decreases with a higher negative slope. After the period ΔD, both currents decrease with the same slope, as expected. The waveforms obtained by simulation are identical to the theoretical waveforms shown in Fig. 5 (c). The current and voltage waveforms on the switches of the bridge a (LV side), b and c (MV side) are presented in the Fig. 9 (e), (f) and (g), respectively. As expected, the semiconductors currents have an offset, leading to the loss of ZCS feature. However, this effect is more relevant on the MV side and less relevant in the LV side. Therefore, it is an advantage for the converter, because the LV bridge, which has higher current and losses, is less affected by the unbalanced power processed by the MV

bridges.

3) Influence of different leakage inductance: To evaluate the sensitivity of the converter to parameter variation, simulation results taking into account deviation on the leakage inductance are obtained and they are presented in Fig. 9 (h) and (i). In this simulation, the leakage inductance of the bridge c was kept constant ($L_c = L = 12.5\mu H$) and it was assumed a deviation of 10% on the leakage inductance of the bridge b and d. In this assumption, the bridge b has lower inductance ($L_b = 0.9L = 11.25\mu H$), while the bridge d has higher leakage inductance ($L_d = 1.1L = 13.75\mu H$). The influence of the inductance deviation on the power processed by the individual bridges is presented in Fig. 9 (h). As expected, the power processed by the bridge b is increased by 10%, resulting in $P_b = 40.7kW$ and the power processed by bridge d is decreased by 10%, resulting in $P_d = 33.3kW$. The power of bridge c remains constant. These values are in agreement with the equation (14) derived in the theoretical analysis. Fig. 9 (h) shows the effect of the leakage inductance variation on the inductors currents. As expected, the currents reach different peak values, because of the different amount of power processed by the MV bridges. Besides that, it is also observed the zero-current-switching operation of the converter. Hence, this result confirms the operation of the converter with soft-switching even taking into account transformer asymmetries.

4) Dynamic operation: Finally, dynamic results are presented in Fig. 10, in order to show the performance of the control structure and also the possibility to process different power by the bridge of the MV side, as described in section IV. For this simulation, a proportional-integral (PI) compensator was used for the output voltage control loop and also for the power balance loop, depicted in Fig. 7. Initially, it was evaluated the possibility to exchange power among the MV bridges. The load connected in the LV side was kept constant and the total power processed by the converter as well. This result is presented in Fig. 10 (a) and, as can be observed, the power processed by the bridges of the MV side changes along the time, while the total power (represented by P_a) remains constant. In the first period (highlighted in that figure), the converter operates with balanced power ($P_b = P_c = P_d$). Then, the operation point of the bridge d is changed, reducing its power by 15%. Consequently, the power processed the other two bridges increase by 7.5%. In the third period, the operation point of all MV bridges changes, so that all bridges process different amount of power, as observed in Fig. 10. In Fig. 10 (b), besides the variation on the power processed by the MV bridges, a load change (total processed power) is also verified. As can be observed in this result, the load is reduced by half. During this moment, the processed power in the MV side remains balanced and the output voltage is well regulated. Therefore, the performance of the control structure described in Section IV is successfully verified.

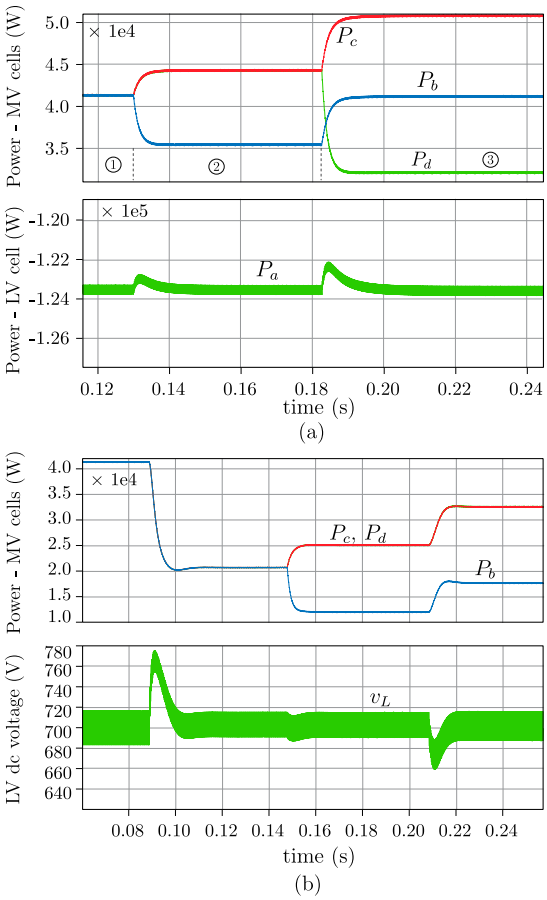

Fig. 10. Simulation results: (a) dynamic operation of the converter, showing variation on the power processed by the MV bridges, for constant load and (b) dynamic behavior for load variation.

VI. Experimental Evaluation

A. Hardware Demonstrator

In order to verify the operation and evaluate the performance of the QAB converter with the TCM experimentally, a down scaled prototype of 2.5 kW was designed, built and tested in laboratory. The primary goal of the prototype is to confirm the analytically studied converter capabilities by experimental results and for that reason a reduced scale prototype was used and the main specifications are presented in Table III. To design the converter, the same design procedure described in Section V (A) was used, taking into account the specifications from Table III. For the experimental set-up, a maximum duty-cycle of $D_{1max} = 0.45$ was chosen and therefore the inductors and the others parameters were selected. Fig. 12 shows the picture of the implemented prototype, where the power board, control board and also the multi-winding transformer are observed. IGBT modules from Infineon were used in all bridges and the specification is also presented in Table III. To control the converter, a Freescale MPC5643L floating point DSP (32-bit CPU, 60MHz) was used. Additional inductors of $35\mu H$ were added to each winding of the transformer, as observed in Fig. 12. The transformer has a U shaped core with ferrite material and it is depicted in Fig. 12 (b). The main parameters were measured and they are presented in Table IV. As can be observed, the leakage inductances have a small deviations among them.

B. Experimental Results

The experimental results consist of relevant voltage and current waveforms for steady-state and dynamic operation of

the QAB converter using the proposed TCM. The main waveforms obtained from the implemented prototype operating at nominal load are shown in Fig. 11 and Fig. 13, and they will be discussed in the following.

1) Steady-State Operation Waveforms: The steady-state waveforms are shown in Fig. 11, and they were obtained by the converter operating at light load condition and nominal conditions. Fig. 11 (a) shows the voltage and current on the bridges a (v_a, i_{La}) and b (v_b, i_{Lb}) for the converter at light load, i.e. $P_a = 1kW$. As can be observed, the duty-cycle is reduced and the zero-time of the currents is very large. Soft-switching is observed and this condition is not critical for the switching. The same waveforms are depicted in Fig. 11 (b) for nominal load condition. The converter has an output power of around 2.5 kW, divided equally among the MV cells. As expected, the current and voltage waveforms are very similar to the theoretical waveforms and the ZCS feature can be noticed in the figure. The switching details are depicted in Fig. 11 (c). Although the zero-time of the current is very short in this condition (worst condition), the ZCS operation is still achieved and confirmed by this result. The waveforms obtained experimentally are very similar to the theoretical waveforms described in section II and to those obtained through simulation. Fig. 11 (d) shows the results for unbalanced condition, where the bridges b and d operate with 640 W, while the bridge c processes 480 W, resulting in a total power of approximately 1.8 kW. For safety reasons, the test was performed with voltage of 150 V in the secondary side. As can be seen in this picture, the bridges b and c have different duty-cycle and this difference is determined by $\Delta D = D_c - D_b$. During the period given by ΔD, the currents i_{La} and i_{Lb} change their slope and i_{Lb} increases instead to decrease. This is explained by the additional level on the voltage v_x, as already described in section IV (A). After the period ΔD, both currents decrease again. Furthermore, it is noticed in this results that the ZCS feature is lost.

TABLE III
SPECIFICATION OF THE IMPLEMENTED DC-DC CONVERTER PROTOTYPE

Parameter	Value
Rated Output Power	$P_o = 2.5kW$
LV dc-link (V_L)	$V_L = 200V$
MV dc-link (V_{Mb}, V_{Mc}, V_{Md})	$V_M = 250V$
Switching frequency	$f_s = 20kHz$
Additional external inductance	$L_a = L_b = L_c = L_d = 35\mu H$
Transformer turns ratio	$n = 1:1:1:1$
Output filter capacitor	$C = 500\mu F$
IGBT $S_{1,2,3,4}$	Infineon SIGC32T120R3E IGBT3 (1200V/25A)

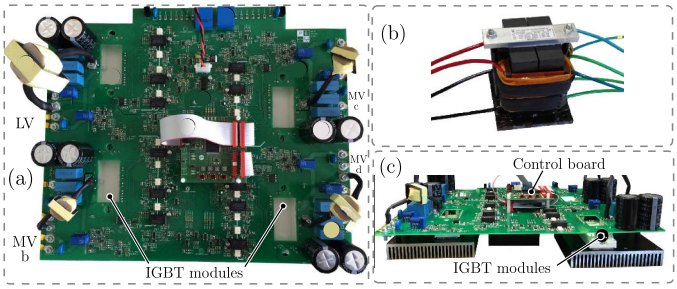

Fig. 12. Picture of the implemented prototype: (a) top-view of the converters prototype, (b) HF multi winding transformer, (c) front-view of the converter.

2) Evaluation of Transformer Parameters Variation: In order to verify experimentally the sensitivity to the transformer leakage inductance, deviation on the leakage inductor was introduced and the converter operation was evaluated. The bridges b and c are used for comparison purpose. The leakage inductance of the bridge c was kept constant ($L_c = L$), while an additional inductance of $10\mu H$ was added in series with L_b, i.e. $L_b = L + 10\mu H$. The currents i_{Lb} and i_{Lc} were saved and

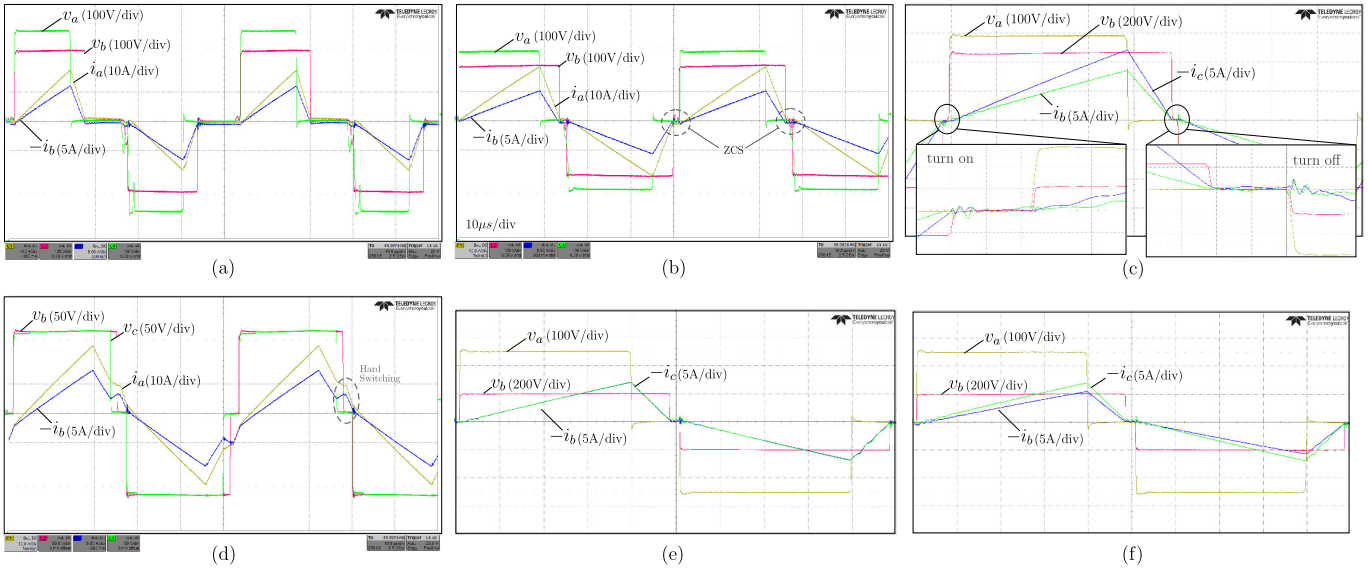

Fig. 11. Experimental result of the QAB converter: (a) operation in steady-state at light load condition, (b) operation in nominal load and balanced condition, (c) switching detail, showing the operation of the converter at ZCS, (d) operation at unbalanced condition, (e) currents waveforms of the bridges b and c, for leakage inductance and (f) for different leakage inductance, showing the effect of the parameter variation on the current waveform.

TABLE IV
MEASURED PARAMETERS OF THE HF MULTIWINDING TRANSFORMER

Parameters	inductance	Resistance
Magnetizing	$L_M = 4.03mH$	$R_M = 102.8k\Omega$
Series parameters		
Winding	inductance	Resistance
a (LV)	$L_{a_{leak}} = 2.67\mu H$	$R_{a_{leak}} = 26.7m\Omega$
b (MV)	$L_{b_{leak}} = 29.97\mu H$	$R_{b_{leak}} = 83m\Omega$
c (MV)	$L_{c_{leak}} = 22.5\mu H$	$R_{c_{leak}} = 59.4m\Omega$
d (MV)	$L_{d_{leak}} = 9.6\mu H$	$R_{d_{leak}} = 77.6m\Omega$

compared and they are show in Fig. 11 (e) and (f). In Fig. 11 (e), the bridges have the same inductance $L_b = L_c = L$, and then the currents i_{Lb} and i_{Lc} are equal. In Fig. 11 (f), the additional inductance is introduced and the power processed by the bridge b is reduced. This reduction is observed on the waveform of the current i_{Lb}, which is also reduced. It is important to highlight that the ZCS feature is still obtained even with the parameter variation.

3) Transient Operation Waveforms: Finally, dynamic results were obtained for power variation of the MV bridges. The output voltage and also the currents on the dc side of the bridges b, c and d were saved in order to show the power processed by these bridges. The transient results are shown in Fig. 13. The unbalanced power condition is evaluated in these results. Fig. 13 (a) shows the waveforms for the converter processing balanced power (i.e. $P_b = P_c = P_d$) and then, due to the control action, the converter operates with different power levels in the MV bridges. As can be seen in this result, the power processed by bridges b and d are reduced, while the power processed by bridge c is increased. Similarly, Fig. 13 (b) shows also the power transient in the converter, but taking into account that the converter was already processing unbalanced power. Initially, the power processed by the bridge d is already higher than the other two bridges. Then, the power P_b is reduced to almost zero, while the power P_c is increased. During this transient, the power of the bridge d remains constant. Thus, these results have confirmed the possibility to exchange power among the MV bridges and validate the control structure presented in Fig. 7 (b).

VII. CONCLUSION

In the framework of SST development, modular architectures will play a fundamental role. In this paper, a quadruple active bridge converter is employed as a basic cell of the dc-dc conversion stage of the SST. The QAB converter has the same features of the DAB converter (as soft-switching and high power density), with the additional characteristic to reduce the number of the HF transformer, since the QAB converter connects more active bridges to a single transformer.

To modulate the converter, the triangular current modulation (TCM) previous studied only for the DAB converter was applied to the QAB converter. This modulation strategy has the advantage to operate with zero-current-switching for a wide range of load and voltage, reducing significantly the switching losses of the converter.

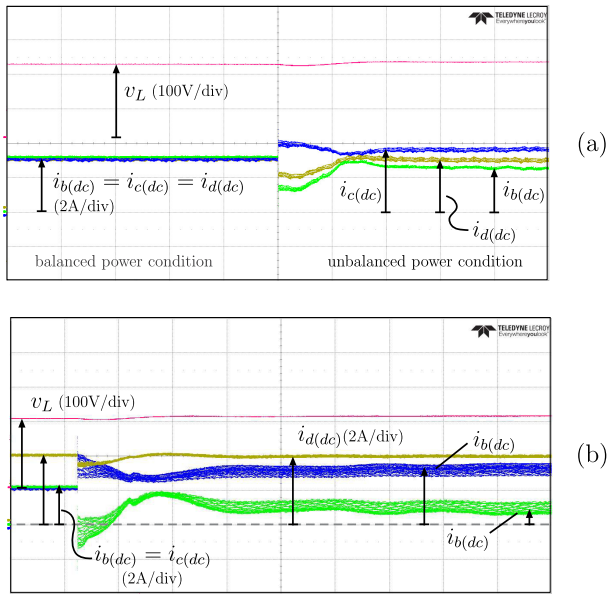

Fig. 13. Experimental result of the QAB converter operating under transient condition, showing the possibility to exchange power among the bridges b, c and d: output voltage and current on the dc side of the bridges b, c and d.

The basic operation of the converter using the TCM was described and all the main equations have been analytically derived and experimentally verified. It was demonstrated in this paper that the ZCS feature is lost in case of unbalanced load of the MV cells. On the other hand, LV bridge, which has higher current and losses, is less affected by the imbalance.

Additionally, a non-ideal transformer (different leakage inductances) was considered in the theoretical analysis. It was demonstrated analytically and experimentally that the leakage inductances deviation has no influence on the soft-switching operation of the QAB converter, but only a small influence on the transferred power.

Finally, the capability of the QAB converter to manage the power exchange among the MV cells has been successfully demonstrated experimentally.

REFERENCES

[1] X. She, A. Q. Huang, and R. Burgos, "Review of solid-state transformer technologies and their application in power distribution systems," *IEEE Journal of Emerging and Selected Topics in Power Electronics*, vol. 1, no. 3, pp. 186–198, Sept 2013.

[2] X. She, X. Yu, F. Wang, and A. Q. Huang, "Design and demonstration of a 3.6-kv 120-v/10-kva solid-state transformer for smart grid application," *IEEE Trans on Power Elect*, vol. 29, no. 8, pp. 3982–3996, Aug 2014.

[3] K. Mainali, A. Tripathi, S. Madhusoodhanan, A. Kadavelugu, D. Patel, S. Hazra, K. Hatua, and S. Bhattacharya, "A transformerless intelligent power substation: A three-phase sst enabled by a 15-kv sic igbt," *IEEE Power Electron Magazine*, vol. 2, no. 3, pp. 31–43, Sept 2015.

[4] J. Clare, "Advanced power converters for universal and flexible power management in future electricity networks," in *European Conf. on Power Electron. and Appl. (ECCE-Europe)*, Sept 2009, pp. 1–29.

[5] S. Bifaretti, P. Zanchetta, A. Watson, L. Tarisciotti, and J. C. Clare, "Advanced power electronic conversion and control system for universal and flexible power management," *IEEE Trans on Smart Grid*, vol. 2, no. 2, pp. 231–243, June 2011.

[6] J. W. Kolar and G. Ortiz, "Solid-state-transformers: Key components of future traction and smart grid systems," in *Proc. of the International Power Electron. Conf.*, May 2014.

[7] M. Liserre, G. Buticchi, M. Andresen, G. D. Carne, L. F. Costa, and Z. X. Zou, "The smart transformer: Impact on the electric grid and technology challenges," *IEEE Industrial Electronics Magazine*, vol. 10, no. 2, pp. 46–58, Summer 2016.

[8] M. Liserre, M. Andresen, L. Costa, and G. Buticchi, "Power routing in modular smart transformers: Active thermal control through uneven loading of cells," *IEEE Industrial Electronics Magazine*, vol. 10, no. 3, pp. 43–53, Fall 2016.

[9] G. D. Carne, M. Liserre, and C. Vournas, "On-line load sensitivity identification in lv distribution grids," *IEEE Transactions on Power Systems*, vol. PP, no. 99, pp. 1–1, 2016.

[10] R. W. D. D. N. Soltau, R. U. Lenke, "High-power dc-dc converter," Technical Report, Rheinisch-Westflische Technische Hochschule, 2013.

[11] S. Madhusoodhanan, A. Tripathi, D. Patel, K. Mainali, A. Kadavelugu, S. Hazra, S. Bhattacharya, and K. Hatua, "Solid-state transformer and mv grid tie applications enabled by 15 kv sic igbts and 10 kv sic mosfets based multilevel converters," *IEEE Trans. on Ind. App.*, vol. 51, no. 4, pp. 3343–3360, July 2015.

[12] D. Rothmund, J. Huber, and J. Kolar, "Operating behavior and design of the half-cycle discontinuous-conduction-mode series-resonant-converter with small dc link capacitors," in *Workshop on Control and Modeling for Power Electronics (COMPEL)*, June 2013, pp. 1–9.

[13] D. Dujic, G. Steinke, E. Bianda, S. Lewdeni-Schmid, C. Zhao, and J. Steinke, "Characterization of a 6.5kv igbt for medium-voltage high-power resonant dc-dc converter," in *IEEE Appl. Power Electron. Conf. and Expo.*, March 2013, pp. 1438–1444.

[14] D. Dujic, A. Mester, T. Chaudhuri, A. Coccia, F. Canales, and J. Steinke, "Laboratory scale prototype of a power electronic transformer for traction applications," in *European Conference on Power Electronics and Applications (ECCE-Europe)*, Aug 2011, pp. 1–10.

[15] C. Zhao, D. Dujic, A. Mester, J. Steinke, M. Weiss, S. Lewdeni-Schmid, T. Chaudhuri, and P. Stefanutti, "Power electronic traction transformer;medium voltage prototype," *IEEE Trans. on Ind. Electron.*, vol. 61, no. 7, pp. 3257–3268, July 2014.

[16] L. Costa, G. Buticchi, and M. Liserre, "A fault-tolerant series-resonant dc-dc converter," *IEEE Transactions on Power Electronics*, vol. 32, no. 2, pp. 900–905, Feb 2017.

[17] X. She, S. Lukic, A. Huang, S. Bhattacharya, and M. Baran, "Performance evaluation of solid state transformer based microgrid in freedm systems," in *IEEE Appl. Power Electron. Conf. and Expo.*, March 2011, pp. 182–188.

[18] H. Fan and H. Li, "High-frequency transformer isolated bidirectional dc-dc converter modules with high efficiency over wide load range for 20 kva solid-state transformer," *IEEE Trans. on Power Electron.*, vol. 26, no. 12, pp. 3599–3608, Dec 2011.

[19] B. Zhao, Q. Song, and W. Liu, "A practical solution of high-frequency-link bidirectional solid-state transformer based on advanced components in hybrid microgrid," *IEEE Trans. on Ind. Electron.*, vol. 62, no. 7, pp. 4587–4597, July 2015.

[20] H. Tao, J. Duarte, and M. Hendrix, "Three-port triple-half-bridge bidirectional converter with zero-voltage switching," *IEEE Trans. on Power Electron.*, vol. 23, no. 2, pp. 782–792, March 2008.

[21] S. Falcones, R. Ayyanar, and X. Mao, "A dc-dc multiport-converter-based solid-state transformer integrating distributed generation and storage," *IEEE Trans on Power Elect*, vol. 28, no. 5, pp. 2192–2203, May 2013.

[22] N. Schibli, "Symmetrical multilevel converters with two quadrant dc-dc feeding," dissertation, Swiss Federal Institute of Technology, 2000.

[23] G. Ortiz, D. Bortis, J. Kolar, and O. Apeldoorn, "Soft-switching techniques for medium-voltage isolated bidirectional dc/dc converters in solid state transformers," in *IECON 2012 - 38th Annual Conference on IEEE Industrial Electronics Society*, Oct 2012, pp. 5233–5240.

[24] H. Zhou and A. Khambadkone, "Hybrid modulation for dual-active-bridge bidirectional converter with extended power range for ultracapacitor application," *IEEE Trans. on Ind. Appl.*, vol. 45, no. 4, pp. 1434–1442, July 2009.

[25] L. F. Costa, G. Buticchi, and M. Liserre, "Quad-active-bridge as cross-link for medium voltage modular inverters," in *IEEE Energy Conversion Congress and Exposition (ECCE)*, Sept 2015, pp. 645–652.

[26] G. Buticchi, M. Andresen, L. Costa, and M. Liserre, "Modular dc/dc converter structure with multiple power flow paths for smart transformer applications," in *European Conference on Power Electronics and Applications (ECCE-Europe)*, Sept 2015, pp. 1–9.

[27] L. F. Costa, G. Buticchi, and M. Liserre, "Comparison of basic power cells for quad-active-bridge dc-dc converter in smart transformer," in *European Conference on Power Electronics and Applications (ECCE-Europe)*, Sept 2015, pp. 1–10.

[28] F. Kieferndorf, U. Drofenik, F. Agostini, and F. Canales, "Modular pet, two-phase air-cooled converter cell design and perfomance evaluation with 1.7kv igbts for mv applications," in *IEEE Appl. Power Electron. Conf. and Expo.*, Sept 2016, pp. 437–479.

Levy Ferreira Costa (S'14) received the B.S. degree in electrical engineering from the Federal University of Ceara, Brazil, in 2010 and the M.S. degree from the Federal University of Santa Catarina, Brazil, in 2013. From 2013 to 2014, he was an Electrical Design Engineer with Schneider Electric, Brazil. He is currently working toward the Ph.D. degree at the Chair of Power Electronics, Christian-Albrechts-University of Kiel, Germany. His research interests include dc-dc converters, UPS systems and high-power converter systems.

Giampaolo Buticchi (S'10-M'13) was born in Parma, Italy, in 1985. He received the Masters degree in Electronic Engineering in 2009 and the Ph.D degree in Information Technologies in 2013 from the University of Parma, Italy. He is now working as a postdoctoral research associate at the University of Kiel, Germany. His research area is focused on power electronics for renewable energy systems, smart transformer fed micro-grids and reliability in power electronics.

Marco Liserre (S'00-M'02-SM'07-F'13) received the M.Sc. and Ph.D degree in Electrical Engineering from the Bari Polytechnic, respectively in 1998 and 2002. He has been Associate Professor at Bari Polytechnic and Professor in reliable power electronics at Aalborg University (Denmark). He is currently Full Professor and he holds the Chair of Power Electronics at Christian-Albrechts-University of Kiel (Germany). He has published over 280 technical papers (more than 70 of them in international peer-reviewed journals), 4 chapters of a book and a book (Grid Converters for Photovoltaic and Wind Power Systems, ISBN-10: 0-470-05751-3 IEEE-Wiley, second reprint, also translated in Chinese). These works have received more than 16000 citations. Marco Liserre is listed in ISI Thomson report The world's most influential scientific minds from 2014. He has been awarded with an ERC Consolidator Grant for the project 'The Highly Efficient And Reliable smart Transformer (HEART), a new Heart for the Electric Distribution System. He is member of IAS, PELS, PES and IES. He is Associate Editor of the IEEE Transactions on Industrial Electronics, IEEE Industrial Electronics Magazine, IEEE Transactions on Industrial Informatics, where he is currently Co-Eic, IEEE Transactions on power electronics and IEEE Journal of Emerging and Selected Topics in Power Electronics. He has been Founder and Editor-in-Chief of the IEEE Industrial Electronics Magazine, Founder and the Chairman of the Technical Committee on Renewable Energy Systems, Co-Chairman of the International Symposium on Industrial Electronics (ISIE 2010), IES Vice-President responsible of the publications. He has received the IES 2009 Early Career Award, the IES 2011 Anthony J. Hornfeck Service Award, the 2014 Dr. Bimal Bose Energy Systems Award, the 2011 Industrial Electronics Magazine best paper award and the Third Prize paper award by the Industrial Power Converter Committee at ECCE 2012, 2012. He is senior member of IES AdCom. In 2013 he has been elevated to the IEEE fellow grade with the following citation "for contributions to grid connection of renewable energy systems and industrial drives".